

B2000 Application Examples

Numerical simulation of the mechanical and optical properties of solid-state laser rods

S. Merazzi
SMR SA
CP 4014
CH-2500 Bienne 4

The numerical simulation of the mechanical and optical properties of solid-state laser rods illustrates the capability of the presented open system to deal with various field problems arising in physics and engineering. A numerical simulation of the thermal, the mechanical and the optical behaviour of end-pumped solid-state lasers based on finite element and finite difference methods is presented. Experimental data are to be found in Pfistner et. al. (1992).

1 Introduction

Solid-state lasers (Koechner 1976) in the power range of 10W to 100W offer a wide range of industrial and scientific applications, such as material processing, laser surgery and spectroscopy. Conventional solid-state lasers pumped by flash lamps normally have a low degree of efficiency in addition to bad beam quality. With today's commercially available high power diode lasers, longitudinal diode pumping of solid-state lasers has become much more interesting, since it offers more efficient laser operation together with high beam quality. Although longitudinal pumping reduces the overall heat load on the laser material (compared to conventional flash lamp pumped systems), thermally-induced beam distortions remain a major problems. For most applications, however, a good beam quality is mandatory for efficient operations. The thorough study of thermal problems is therefore one of the main concerns in designing solid-state lasers.

The following presentation aims at establishing a numerical simulation of diode-pumped solid-state lasers, in order to predict their performance. Results obtained from the numerical models are discussed, experimental data being presented in the paper by Pfistner et al. (1992). In addition, the system's capability to deal with coupled field problems is briefly exposed.

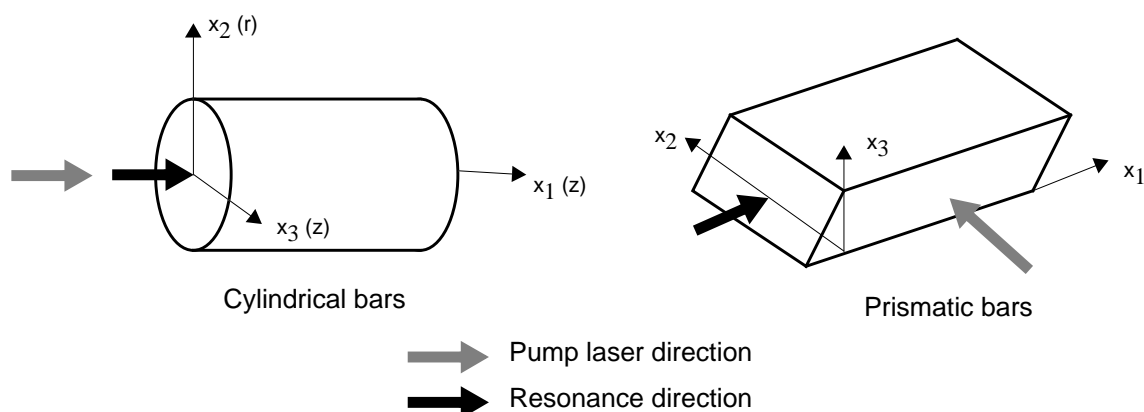


Figure 1: Schematic display of typical laser resonator crystal specimens.

The numerical simulation of the behaviour of diode-pumped solid-state lasers can be divided into three sub-problems:

1. *Calculation of the heat deposited in the laser:* A ray-tracing method is used to calculate the heat deposited by the pump laser(s) in the laser.
2. *Analysis of the thermal behaviour of the crystal under the steady-state heating induced by the pump laser:* Variations in temperature create stresses in the crystal inducing a variable index of refraction due to thermal dispersion.
3. *Analysis of the deformations and the stresses in the crystal due to the heating induced by the laser light:* Deformations of the surface change the reflective properties of the crystal, thus introducing aberrations. Stresses induce additional modifications of the index of refraction due to the elasto-optic effect.
4. *Analysis of the optical performance:* As a consequence of the changes of the refractive index field calculated in steps 1 and 2, the steady-state laser field can be computed by means of the method of resonant excitation (Frauchiger).

The specimens studied are cylindrical and prismatic bars (see figure 1). Depending on the material properties the cylindrical bars may be studied assuming axisymmetry. Typical materials are Nd:YAG, Nd:GSGG and Nd:YLF materials. The material properties are listed in table 1. Nd:YLF has isotropic mechanical properties, but the thermal expansion coefficients are orthotropic.

The thermal conductivity properties of all materials studied are isotropic, but the conductivity coefficient is a function of the temperature (see figure 2). The nonlinear thermal conductivity effect will be small for materials that exhibit a small temperature rise. However, for materials like Nd:GSGG the effect is quite considerable: The non-linear behaviour leads to an augmentation of the temperature of around 25% compared to the linear solution. Consequently, stresses will also increase significantly.

Figure 2: Thermal conductivity of GSGG/YLF material as a function of the ambient temperature.

Thermal conductivity function:

$$k_{eff}(T) = k \frac{300}{300 + T} \quad \text{Eq. 1}$$

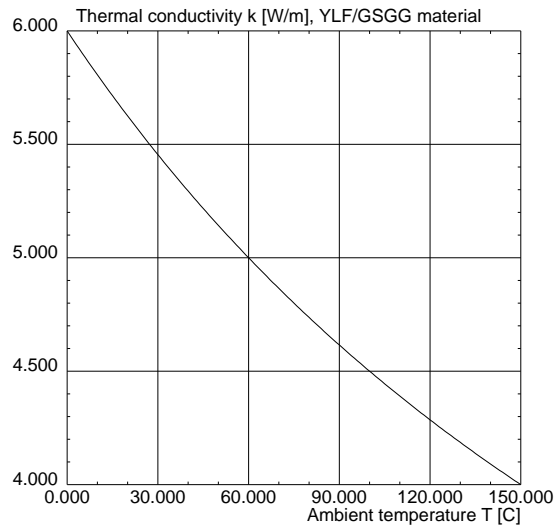


Table 6-1 Material constants

Material property	Nd:GSGG	Nd:YLF	Nd:YAG
Thermal conductivity k [W m ⁻¹ K ⁻¹] (All materials are isotropic)	6	6	13

Table 6-1 Material constants

Material property	Nd:GSGG	Nd:YLF	Nd:YAG
Thermal expansion coefficient α_T [K^{-1}]	6.9×10^{-6}	13×10^{-6} , 8×10^{-6}	8.2×10^{-6}
Modulus of elasticity E [MPa]	210000	75000	310000
Poisson ratio ν	0.28	0.33	0.3
Absorption coefficient α [m^{-1}]	0.227	0.045	0.091
Index of refraction n	1.94	1.47 / 1.448	
$\frac{\partial n}{\partial T}$ at 300 K ($\times 10^{-6} K^{-1}$)	10.5	-4.3/-2.0	7.3
Elasto-optical coefficients p_{11}, p_{12}, p_{44}	-0.012, 0.019, -0.0665		-0.029, 0.0091, -0.0615
Pump waist radius [m]	125×10^{-6}	125×10^{-6}	125×10^{-6}
Laser wavelength [nm]	1062	1047/1053	1064
Pump laser wavelength [nm]	809	797	809

This multi-physics problem is data driven, i.e. as soon as certain data is available a new module can be started. Figure 3 schematically displays the order of the operations. First, a mesh is produced. The heat deposition module then computes the heat at each node of the mesh due to the pump laser(s). This heat vector is then piped in the thermal analysis module which produces a temperature distribution at the nodes of the thermal analysis computational mesh. Figure 4 shows a typical input to the B2000 Input Processor. Once the thermal problem is solved the data base contains the temperature distribution at the mesh nodes. This information is transmitted to the deformation analysis module, together with the description of the mesh (which is the same as for the temperature analysis problem). The stress analysis module reads the temperature distribution data objects and computes the equivalent nodal forces resulting from the thermal pre-stress. The nodal forces become the right-hand side of the stress analysis problem. Displacements, strains and stresses are computed by the stress analysis module. All data needed to run the optical propagation module, i.e. temperatures, displacements, strains, and stresses are now available. Since strains and stresses are computed element-wise at the element integration points they have to be extrapolated to the mesh nodes. All nodal values are then interpolated to the optical mesh. Temperatures and strains will be used to compute the variable index of refraction. The displacements will be used to compute update coordinates for the propagation of the electrical field.

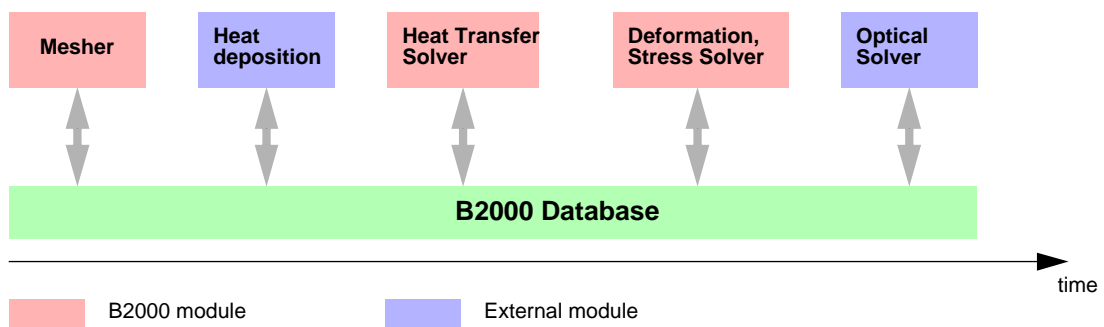


Figure 3: Schematic view of modules and data flow during solid-state multi-physics Laser analysis.

```

# Parametrize geometry and discretization:

{Radius=0.0015} {Length=0.005}
{Nrow=41} {Ncol=21}

title 'Cylindrical YAG crystal [w,m,kg,N,C]'
# define subdomain 1
branch 1
# element patch is rectangular plate
patch nolist
  geom plate
  nrow {Nrow} ncol {Ncol}
  type Q8_ALAP mid 1 nint=2
  p1 0. 0. 0.
  p2 {Length} 0. 0.
  p3 {Length} {Radius} 0.
  p4 0. {Radius} 0.
endpatch
# Dirichlet boundary conditions on last row
bound
  val 0. dof 1 {Nrow*Ncol-1}+1/{Nrow*Ncol}
endbound
endbranch
# element material constants
ematerial
  mid 1
  type laplace k 13.
endmid
endmaterial
run

```

Figure 4: Input description of thermal problem.

2 Thermal analysis

The thermal analysis of resonators is modeled by means of the steady-state heat-conductivity equation (Poisson equation) with non-linear conductivity coefficients

$$\frac{\partial}{\partial x_1} \left(k_1(T) \cdot \frac{\partial T}{\partial x_1} \right) + \frac{\partial}{\partial x_2} \left(k_2(T) \cdot \frac{\partial T}{\partial x_2} \right) + \frac{\partial}{\partial x_3} \left(k_3(T) \cdot \frac{\partial T}{\partial x_3} \right) = q_v \quad \text{Eq. 2}$$

$$T = T_c \quad \text{on the boundary } \Gamma_c$$

$$k_n(T) \frac{\partial T}{\partial n} = q_s \quad \text{on the boundary } \Gamma_s \quad \text{Eq. 3}$$

T stands for the temperature and q_v and q_s for the heat per volume or per surface unit. k_i denotes the thermal conductivity along the i -th axis and k_n the thermal conductivity in an arbitrary direction n . The steady-state boundary conditions consist of constant temperature values (Dirichlet conditions on boundary Γ_c) and convection conditions (Neumann conditions) on the boundary Γ_s (Newton's law of cooling):

$$q_s = h(T_\infty - T) \quad \text{Eq. 4}$$

T_∞ designates the surrounding temperature. To formulate the standard isoparametric elements we start from the functional which is obtained by multiplying Eq. 2 with T and by integrating by parts:

$$\Pi = \int_{\Omega} \left[k_1 \left(\frac{\partial T}{\partial x_1} \right)^2 + k_2 \left(\frac{\partial T}{\partial x_2} \right)^2 + k_3 \left(\frac{\partial T}{\partial x_3} \right)^2 \right] dV - \int_{\Omega} T q_v dV - \int_{\Gamma_c} T q_s n dS \quad \text{Eq. 5}$$

The first expression stands for the potential energy stored in the body Ω and the second and the third ones for the external energy. The third expression describes the heat transfer on the body surface Γ_s . Assuming constant coefficients k the variation $\delta\Pi = 0$ leads to the form

$$\begin{aligned} \delta\Pi &= \int_{\Omega} \left[\frac{\partial \delta T}{\partial x_1} k_1 \frac{\partial T}{\partial x_1} + \frac{\partial \delta T}{\partial x_2} k_2 \frac{\partial T}{\partial x_2} + \frac{\partial \delta T}{\partial x_3} k_3 \frac{\partial T}{\partial x_3} \right] dV \\ &+ \int_{\Omega} \delta T q_v dV - \int_{\Gamma_c} \delta T q_c dV - \int_{\Gamma_s} \delta T h (T_{\infty} - T) dS = 0 \end{aligned} \quad \text{Eq. 6}$$

with $dV = dx_1 dx_2 dx_3$

Eq. 6 is now integrated in discrete form by means of the isoparametric approximations of the coordinates and of the temperature field defining the element

$$T = \sum_{i=1,nn} T_i \varphi_i \quad \text{Eq. 7}$$

The thermal analysis process by means of finite elements is well known (see for instance Bathe 1982). It will be illustrated here for the derivation of the radiation boundary condition elements, i.e. the last integral expression in Eq. 6, since the latter add contributions to the discrete operator. The integration will therefore be performed over the surface only, i.e. $dx_3 = 0$. The surface of the radiation element is approximated by

$$\mathbf{r} = \sum_{i=1,nn} \mathbf{r}_i \varphi_i \quad \text{Eq. 8}$$

The base vectors $\hat{\mathbf{g}}_{\alpha}$ of any point on the surface then become

$$\mathbf{g}_{\alpha} = \frac{\partial \mathbf{r}}{\partial \theta_{\alpha}} = \sum_{i=1,nn} \mathbf{r}_i \frac{\partial \varphi_i}{\partial \theta_{\alpha}} \quad \alpha = 1, 2 \quad \text{Eq. 9}$$

and the infinitesimal surface element

$$\begin{aligned} dS &= g d\theta_1 d\theta_2 \quad \alpha = 1, 2 \\ g &= |g_{\alpha\beta}| = \sqrt{g_{11}g_{22} - g_{12}g_{21}} \end{aligned} \quad \text{Eq. 10}$$

Substitute Eq. 8 and Eq. 10 in last expression of Eq. 6

$$-\int_S \delta T h (T_{\infty} - T) dS = \int_S \varphi_i h \varphi_j g d\theta_1 d\theta_2 - \int_S \varphi_i h \varphi_j T_{\infty} g d\theta_1 d\theta_2 \quad \text{Eq. 11}$$

The first term to the right of Eq. 11 can be formulated as one-dimensional elements during axisymmetric analysis and as four to eight node two-dimensional surface elements (see figure 5). The second term to the right of Eq. 37 is added to the source terms.

The inner heat generated by the pump laser, i.e. the pump distribution, is modeled by means of the source term

$$q_v = f(x_1, x_2, x_3) \quad \text{Eq. 12}$$

and the expression for the heat distribution may either be introduced as a procedure which is compiled in the code, or as an expression which will be evaluated while the input data are compiled. The heat source is proportional to the pump laser light absorption. A typical heat source for the cylindrical specimen based on a Gaussian distribution is given below:

$$q_V(x_1, x_2, x_3) = \frac{2Q\alpha}{\pi\omega_p^2} (1 - \exp(-\alpha l)) \exp\left(\frac{-2x_2^2}{\omega_p^2}\right) \exp(-\alpha x_1) \tag{Eq. 13}$$

α denotes the thermal absorption coefficient of light and ω_p the pump laser light frequency. Q is the thermal power absorbed by the crystal per unit volume (heat load) and l is the length of the rod. Figure 5 displays the mesh geometry and the boundary conditions for a 3D case. Figure 6 shows the distribution of heat source $q_V(x_i)$ generated by the pump function $s(x_i)$.

The solution of the problem, i.e. the temperature field T , is determined by the linear macro-processor (see Chapter 4), if the thermal conductivity k is constant. In case of temperature-dependent thermal conductivity as in Eq. 1 a nonlinear solution procedure must be adopted. The method used here is the modified Newton iteration scheme. This method is sufficient for non-linear behaviour as in Eq. 1 where the tangent matrix is always positive. The modified Newton iteration macro-processor has been mentioned in Chapter 4. It requires the first variation $\delta\Pi$ and the second variation $\delta^2\Pi$ of the expression of the discrete form of Eq. 6. The second variation $\delta^2\Pi$ is computed for the initial step

$$k(T) = k(T_o) = k(0) \tag{Eq. 14}$$

i.e. it corresponds to the linear solution. During the iteration process $k(T)$ is evaluated by means of the current i -th solution T_i

$$k(T) = k(T_i) \tag{Eq. 15}$$

The converged temperature field T in the form of the data object

```
TEMP.ibr...icase
```

is stored on the common data base file ready to be processed by the stress analysis processors. In the case of one single sub-domain and one heat and boundary condition distribution only, it reduces to

```
TEMP.1...1
```

The example solution of a cylindrical model pertains to a Nd:GSGG specimen of length $l=0.005\text{m}$ and radius $r=0.0015\text{m}$. The pump distribution and the temperature distribution for the Nd:GSGG case is shown in figure 5. The effect of the

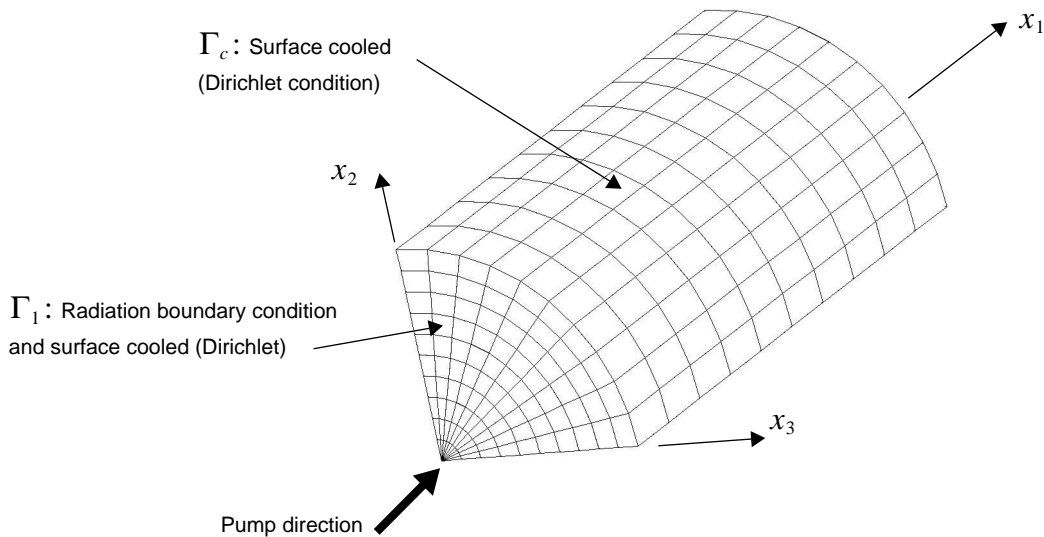


Figure 5: Thermal analysis: Computational mesh and boundary conditions (Nd:YLF)

temperature-dependent thermal conductivity k is non-negligible: For Nd:YLF material the rise in temperature due to temperature-dependent k is about 5.5%. For Nd:GSGG material it increases to about 23%.

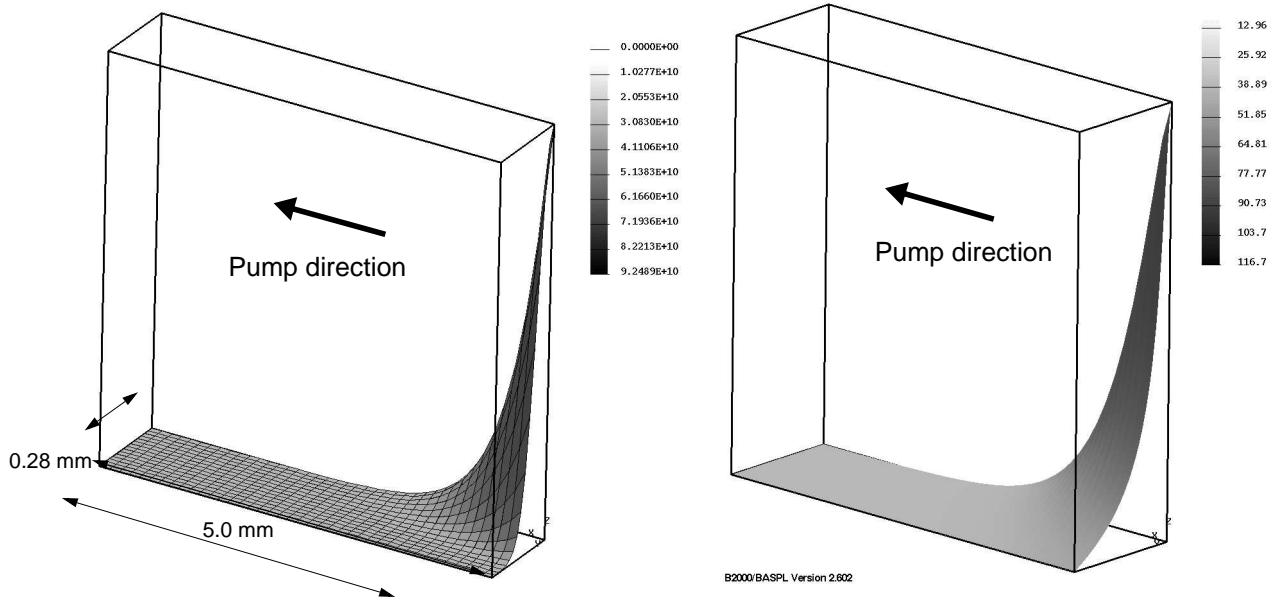


Figure 6: Axisymmetric thermal analysis of Nd:GSGG, front side not cooled. Heat distribution for beam waist radius of 0.125 mm (left). A narrow segment of 0.28 mm is shown, since the heat source is concentrated around the beam axis. Temperature distribution for beam waist radius of 0.125 mm (right).

3 Analysis of deformations and stresses

The numerical model adopted for this application relies on the standard displacement-based finite element method. The standard linear analysis makes use of right-hand side terms (forces) generated by the temperature distribution which has been obtained by the thermal analysis. These forces are caused by the initial stresses $\bar{\sigma}$ which are generated by the thermal expansion $\alpha_i \Delta T$:

$$\sigma_i = E_{ij}(\epsilon_j - \bar{\epsilon}_i) = E_{ij}(\epsilon_j - \alpha_i \Delta T) \quad \text{Eq. 16}$$

In the variational formulation

$$\Pi = \int_V \sigma_{ij} [E_{ijkl}(\epsilon_{kl} - \bar{\epsilon}_{kl})] dV + \text{external energy terms} \quad \text{Eq. 17}$$

the prestress $\bar{\epsilon}_i$ generated by the temperature field can actually be transferred to the right-hand sides s_i

$$s_i = \int_V E_{ij} \cdot \alpha_i \Delta T dV \quad \text{Eq. 18}$$

The standard displacement-based isoparametric formulations for the geometry

$$\mathbf{r} = \sum_{i=1, nnode} \mathbf{r}_i \phi_i \quad \text{Eq. 19}$$

and for the displacement field \mathbf{u}

$$\mathbf{u} = \sum_{i=1, nnode} \mathbf{u}_i \phi_i \quad \text{Eq. 20}$$

lead to four and eight node plane or axisymmetric elements, as well as to eight and twenty node volume elements. These procedures have been well documented (e.g. Bathe 1982). As in the case of thermal analysis, the new elements are introduced in the element and strain processing modules.

Examples of calculations of the thermally-induced stress analysis of an axisymmetric Nd:GSGG rod and the three-dimensional analysis of a Nd:YLF rod:

- The Nd:GSGG material exhibits isotropic thermal expansion behaviour. An axisymmetric analysis is therefore sufficient, and the same mesh as the one for during thermal analysis can be used. Figure 7 displays the initial and the deformed mesh. The deformations on the left face of the cylinder are in the order of 500nm.
- Nd:YLF material has orthotropic thermal expansion coefficients along the two crystal axes x_2 and x_3 . A three-dimensional analysis has therefore been performed in order to evaluate the influence of orthotropic thermal expansion coefficients on the deformation and on the stresses. Due to symmetry a fourth of a cylinder can be modeled. Results of figure 8 confirm the experimental observation, i.e. the deformation is elliptical.

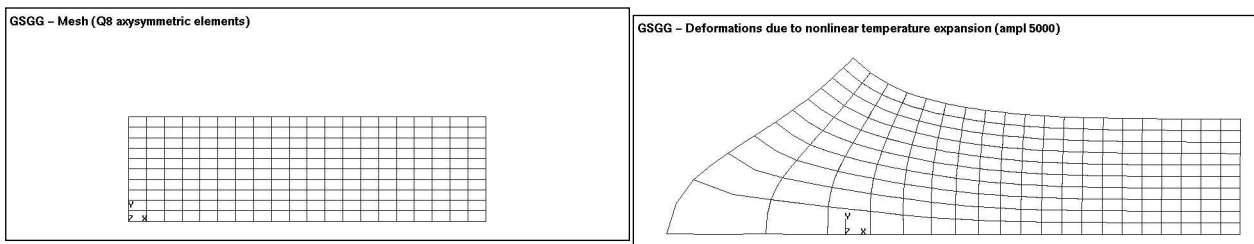
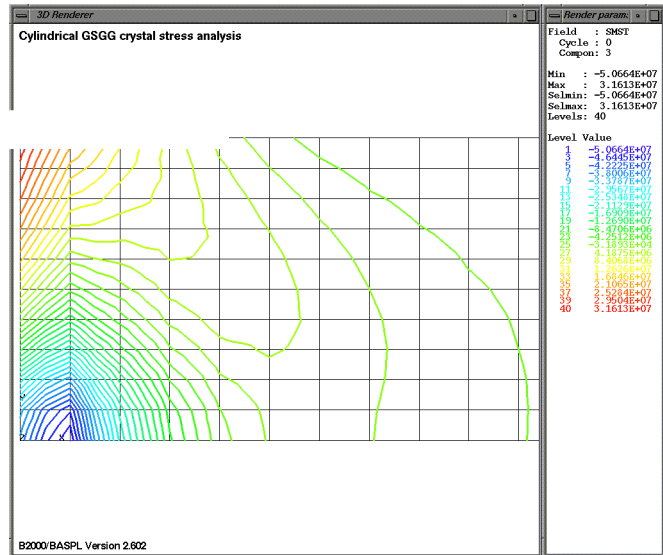


Figure 7: Axisymmetric deformation analysis of Nd:GSGG rod: Initial mesh (left) and deformed mesh (right).

Figure 8: Axisymmetric deformation analysis of a Nd:GSGG rod: Hoop Stress distribution (units in psi).



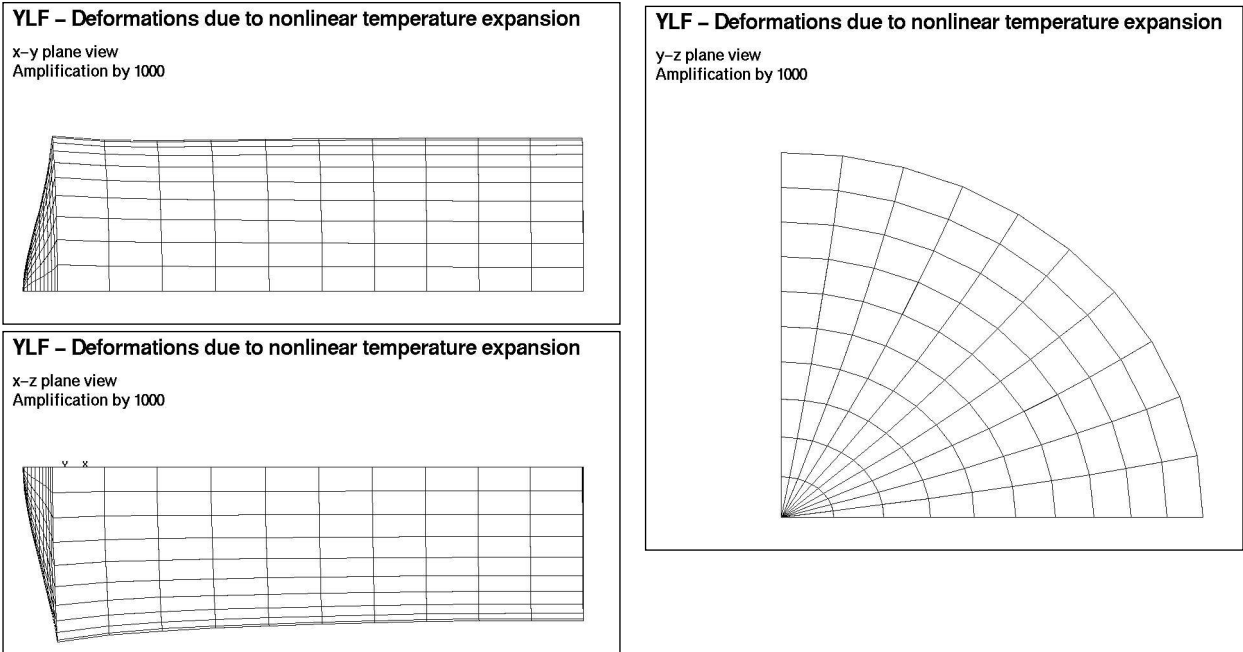
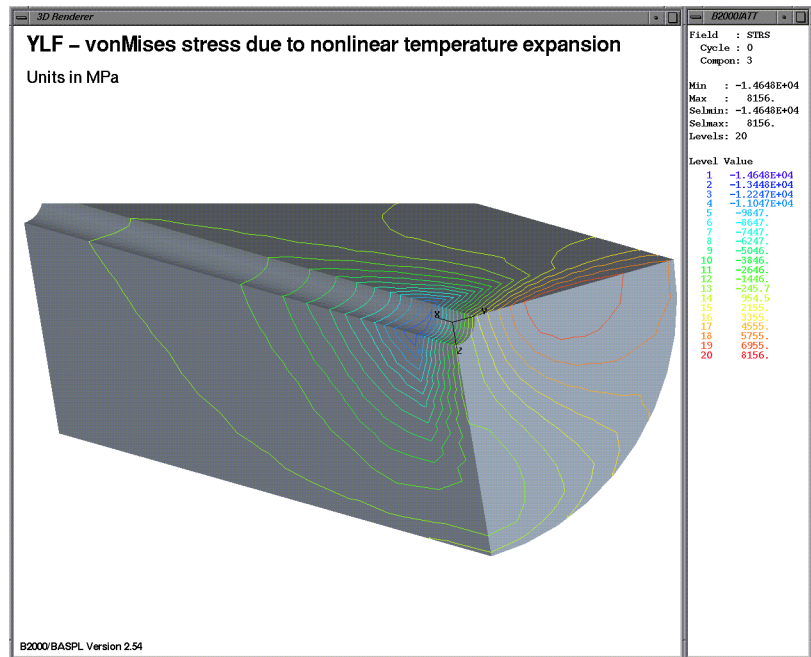


Figure 9: 3-dimensional deformation analysis of Nd:YLF rod due to non-linear thermal behaviour: X-y plane view of deformed mesh (top), x-z plane (middle) and y-z plane (bottom). Deformations are amplified by a factor 1000.

Figure 10: Three-dimensional non-linear thermal deformation analysis of Nd:YLF: Hoop stress distribution (units in MPa).



4 Optical analysis

The optical performance of the laser is studied by propagating a plane wave through the inhomogeneous crystal according to the scalar wave equation (Siegman 1986)

$$\nabla^2 \tilde{E}(x_i) + k^2(x_i) \tilde{E}(x_i) = 0 \quad x = 1, 3 \quad \text{Eq. 21}$$

\tilde{E} represents the complex electromagnetic field. Laser light essentially vibrates at a single frequency, leading to the following assumption for the electrical field

$$\tilde{E} = E_0 \cdot e^{i(\omega t - kx_1)} \quad k = \frac{2\pi}{\lambda} \quad \text{Eq. 22}$$

The field propagates in the direction of x_1 . Eq. 22 is inserted in Eq. 21. The resulting form is also referred to as the paraxial wave equation (2-dimensional case):

$$\frac{\partial^2}{\partial x_1^2} E(x_1, x_2) + \frac{\partial^2}{\partial x_2^2} E(x_1, x_2) = 2ik \frac{\partial}{\partial x_1} E(x_1, x_2) \quad \text{Eq. 23}$$

How are the thermal effects now influencing the above equation? On the one hand there are the crystal deformations, which will be introduced in the numerical model by the coordinates x_i and by the displacement field \mathbf{u} . On the other hand there is the modification of the index of refraction due to the thermal dispersion and the strain-induced birefringence effect:

$$n_{ij} = n_0 + \frac{dn_0}{dT} T + p_{ijkl} \epsilon_{kl} \quad \text{Eq. 24}$$

and

$$k = k_0 n \quad \text{Eq. 25}$$

The calculated strains are related to the index of refraction by the photo-elastic effect

$$\Delta B_{kl} = p_{ijkl} \epsilon_{kl} \quad \text{Eq. 26}$$

The strains are normally computed with respect to the element local or the global coordinate system. In case of axisymmetric analysis, the global coordinate system coincides with the system in which the tensor p_{ijkl} has been defined. Depending on the coordinate system in which the components of p_{ijkl} are defined, a change of reference frame might be necessary.

Cylindrical resonators can be modeled in 2 dimensions by assuming axisymmetry (see figure 1):

$$\begin{aligned} x_1 &= z \\ x_2 &= r \end{aligned} \quad \text{Eq. 27}$$

z and r refer to usual conventions in cylindrical coordinates, while x_i refers to the coordinate system of the numerical analysis program.

$$\frac{\partial^2}{\partial z^2} E(z, r) + \frac{1}{r} \frac{\partial}{\partial r} r \frac{\partial}{\partial r} E(z, r) = 2ik \frac{d}{dz} E(z, r) \quad \text{Eq. 28}$$

The resulting system of coupled equations is obtained by splitting the complex electric field into its real (U) and complex (V) parts:

$$\begin{aligned}
 E(z, r) &= U(z, r) + iV(z, r) \\
 \text{Amplitude: } A &= \sqrt{(U^2 + V^2)} \\
 \text{Phase: } P &= \text{atan}\left(\frac{U}{V}\right)
 \end{aligned}
 \tag{Eq. 29}$$

Eq. 29 is then decomposed into two equations:

$$\begin{aligned}
 \frac{\partial^2 U}{\partial z^2} + \frac{1}{r} \frac{\partial}{\partial r} r \frac{\partial}{\partial r} U &= -2k \frac{\partial}{\partial z} V \\
 \frac{\partial^2 V}{\partial z^2} + \frac{1}{r} \frac{\partial}{\partial r} r \frac{\partial}{\partial r} V &= 2k \frac{\partial}{\partial z} U
 \end{aligned}
 \tag{Eq. 30}$$

The terms

$$\frac{\partial^2 U}{\partial z^2} \quad \text{and} \quad \frac{\partial^2 V}{\partial z^2}$$

are much smaller compared to the derivatives with respect to r and may therefore be neglected:

$$\begin{aligned}
 \frac{1}{r} \frac{\partial}{\partial r} r \frac{\partial}{\partial r} U &= -2k \frac{\partial}{\partial z} V \\
 \frac{1}{r} \frac{\partial}{\partial r} r \frac{\partial}{\partial r} V &= 2k \frac{\partial}{\partial z} U
 \end{aligned}
 \tag{Eq. 31}$$

The discrete form of Eq. 31 result in an unsymmetrical system of equations. A direct solution method is unsuitable in this context, since the resolution needed will create excessive overhead there. A time-marching scheme is therefore chosen (see Richtmyer and Morton 1967). It proves to be the most efficient numerical method. A purely explicit finite difference scheme together with a semi-implicit finite element scheme have been tested. The paraxial wave equation in cylindrical coordinates

$$\left(\begin{aligned}
 \frac{1}{x_2} \frac{\partial}{\partial x_2} x_2 \frac{\partial}{\partial x_2} U(x_1, x_2) &= -2ik \frac{\partial}{\partial x_1} V(x_1, x_2) \\
 \frac{1}{x_2} \frac{\partial}{\partial x_2} x_2 \frac{\partial}{\partial x_2} V(x_1, x_2) &= 2ik \frac{\partial}{\partial x_1} U(x_1, x_2)
 \end{aligned} \right)
 \tag{Eq. 32}$$

is approximated by means of explicit and semi-implicit upwind schemes. To simplify notations we rewrite

$$z = x_1 \quad r = x_2
 \tag{Eq. 33}$$

The operator in the propagation direction is approximated by forward differences (i.e by the mean value over the new interval j):

$$2k \frac{V_{j+1} - V_j}{\Delta z_j} = -\alpha \frac{1}{r} \frac{\partial}{\partial r} r \frac{\partial}{\partial r} U_j + (1-\alpha) \frac{1}{r} \frac{\partial}{\partial r} r \frac{\partial}{\partial r} U_{j+1}
 \tag{Eq. 34}$$

The fully explicit scheme, i.e. $\alpha = 1$, is the most straightforward technique. $\alpha = 1/2$ corresponds to an implicit scheme. With the same expression for U and with $\alpha = 1$ the explicit new values become

$$\begin{aligned}
J_{j+1} &= U_j + \frac{\Delta z_j}{2k} \frac{1}{r} \frac{\partial}{\partial r} r \frac{\partial}{\partial r} V \\
V_{j+1} &= V_j - \frac{\Delta z_j}{2k} \frac{1}{r} \frac{\partial}{\partial r} r \frac{\partial}{\partial r} U_j
\end{aligned}
\tag{Eq. 35}$$

The Laplace operator in r is approximated by central differences

$$\frac{1}{r} \frac{\partial}{\partial r} r \frac{\partial}{\partial r} U = \frac{1}{r_i} \left(\frac{(r_{i+1} + r_i)(U_{i+1} - U_i)}{\Delta r_i (\Delta r_i + \Delta r_{i-1})} - \frac{(r_i + r_{i-1})(U_i - U_{i-1})}{\Delta r_{i-1} (\Delta r_i + \Delta r_{i-1})} \right)
\tag{Eq. 36}$$

and the final discrete system becomes

$$\begin{aligned}
U_{j+1} &= U_j + \frac{\Delta z_j}{2k} \left(\frac{1}{r_i} \left(\frac{(r_{i+1} + r_i)(U_{i+1} - U_i)}{\Delta r_i (\Delta r_i + \Delta r_{i-1})} - \frac{(r_i + r_{i-1})(U_i - U_{i-1})}{\Delta r_{i-1} (\Delta r_i + \Delta r_{i-1})} \right) \right) \\
V_{j+1} &= V_j - \frac{\Delta z_j}{2k} \left(\frac{1}{r_i} \left(\frac{(r_{i+1} + r_i)(U_{i+1} - U_i)}{\Delta r_i (\Delta r_i + \Delta r_{i-1})} - \frac{(r_i + r_{i-1})(U_i - U_{i-1})}{\Delta r_{i-1} (\Delta r_i + \Delta r_{i-1})} \right) \right)
\end{aligned}
\tag{Eq. 37}$$

Assuming a Gaussian intensity distribution at $z = 0$ (Koechner) which models a plane wave with the initial phase equal to zero

$$E(r) = E_0 \cdot \exp\left(-\frac{r^2}{w^2}\right)
\tag{Eq. 38}$$

the initial conditions due to the Gauss beam become

$$\begin{aligned}
U(z = 0) &= 0 \\
V(z = 0) &= E_0 \cdot \exp\left(-\frac{r^2}{w^2}\right)
\end{aligned}
\tag{Eq. 39}$$

The parameter w is called the beam radius. More complex initial conditions like those imposed by pump diode arrays can be modelled easily either by superimposing several Gauss beams or by supplying tabulated values for V .

A semi-implicit finite-element scheme which allows for variable grid size in the radial direction has been studied. It has been discarded, because the variable grid size in the z -direction which results from the deformed geometry requires the block-tridiagonal system to be factored at each pseudo-time step. Thus, the algorithm becomes inefficient, even when compared to the fully explicit scheme.

The purely explicit scheme obviously requires the finest resolution in the propagation direction, but it has the advantage that the variable step size Δz induced by the deformations can be inserted in the scheme. The semi-implicit scheme with variable step size Δz requires the matrix to be factored at each step. Consequently, the semi-implicit method is little cost-effective.

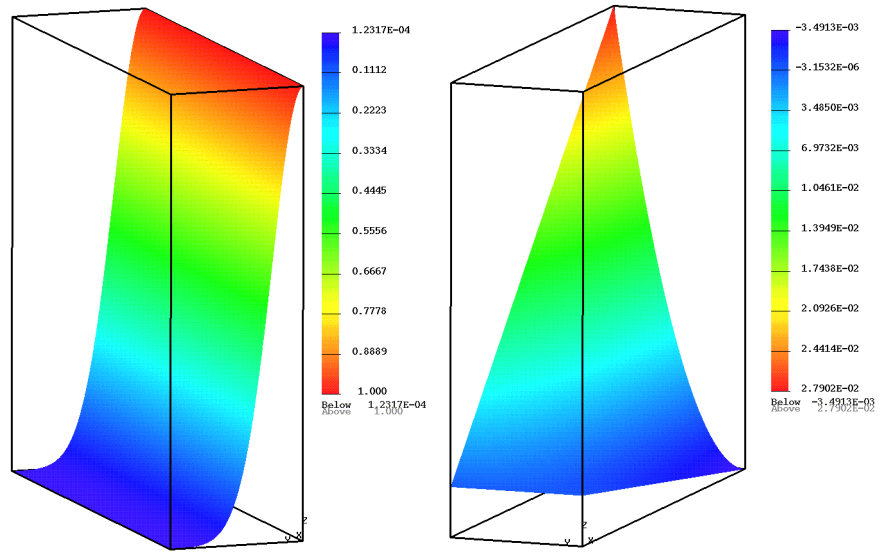
The integration methods are programmed and inserted in the analysis system in the form of a new module. Thereby, several technical problems have to be solved:

- The computational meshes for the thermal analysis as well as for the stress analysis are assumed to be the same meshes made up of linear or quadratic isoparametric elements. Temperatures, displacements and strains/stresses refer to this mesh.
- The optical propagation scheme mesh is much more dense (up to a factor 100) than the meshes used to approximate the thermal problem and the stress problem. The values for the temperature and the strains must therefore be interpolated in the optical mesh.
- It is not reasonable to store all values obtained for the optical mesh. A third mesh is therefore defined for storing,

visualizing and processing of the results of the optical simulation.

Figure 11 displays the distribution of the amplitude for one pass. Detailed information on the numerical experiments as well as some simplifications with respect to the solution of the paraxial wave equation are to be found in Pfistner et. al. (1992).

Figure 11: Propagation analysis:
Distribution of U (left) and V (right) after one pass. pass)



For small angles of divergence, as pointed out in Pfistner et. al. (1992), the influence of energy transport perpendicular to the direction of propagation can be neglected. Thus, the integration can be performed in the direction of propagation only, i.e. r can be kept constant. The optical path difference OPD then becomes, for $r = const$

$$OPD(r) = \int_0^l \frac{\partial n}{\partial T} T(r) dz + n_0 \Delta u(r) + \sum_{i,j=1,3} \int_0^l \frac{\partial n}{\partial \epsilon_{ij}} \epsilon_{ij}(r) dz \tag{Eq. 40}$$

The different sums of Eq. 40 can easily be obtained by extracting the necessary information from the data base files. Data is extracted either by means of the command language or by means of specially written data extraction programs.

5 Conclusion

The methods and the computational modules provide an integrated tool for parametric studies on two- and three-dimensional objects. The individual field problems (thermal analysis, deformation analysis and optical analysis) are integrated by means of the common data base and data structure as well as through the common language.

Parametric studies are performed on specimens with varying material properties and dimensions. While some boundary conditions, like cooled surfaces or optical surfaces, are fixed, other may be varied. Thus, ideas like pre-stressing the crystals, can be studied (prestress the crystal is a way of avoiding tensile cracks in the crystal material). Stress analysis shows that substantial tension stresses build up in the material. Since the materials have better resistance to compressive stresses, prestress will shift stresses towards compression, i.e the maximum compressive stress will increase, whereas the

maximum tensions stresses will decrease. Since the influence of the stresses on the optical behaviour are small, pre-stress will not modify the optical properties significantly.

References

Bathe, K.-J., *Finite element procedures in engineering analysis*, Prentice-Hall (1982).

Koechner W., *Solid state laser engineering*, Springer Verlag New York (1976).

Pfistner Ch., Weber R., Weber H.P., Merazzi S., Gruber R., *Thermal beam distortions in longitudinally pumped solid state lasers*, Paper submitted to IEEE Journal of Quantum Electronics (1992).

Richtmyer R. D., Morton K. W., *Difference methods for initial value problems*, Interscience Publishers, Wiley (1967).

Siegman, A. E., *Lasers*, Oxford University Press (1986).